# Solution X-Ray Scattering-Based Estimation of Electron Cryomicroscopy Imaging Parameters for Reconstruction of Virus Particles

Pamela A. Thuman-Commike,* Hiro Tsuruta,# Barrie Greene,§ Peter E. Prevelige, Jr.,¶ Jonathan King,§ and Wah Chiu*

*Verna and Marrs McLean Department of Biochemistry, Baylor College of Medicine, Houston, TX 77030; #Stanford Synchrotron Radiation Laboratory, Stanford University, Stanford, CA 94309-0210; §Department of Biology, Massachusetts Institute of Technology, Cambridge, MA 02142; and ¶Department of Microbiology, University of Alabama at Birmingham, Birmingham, AL 35294, USA

ABSTRACT Structure factor amplitudes and phases can be computed directly from electron cryomicroscopy images. Inherent aberrations of the electromagnetic lenses and other instrumental factors affect the structure factors, however, resulting in decreased accuracy in the determined three-dimensional reconstruction. In contrast, solution x-ray scattering provides absolute and accurate measurement of spherically averaged structure factor amplitudes of particles in solution but does not provide information on the phases. In the present study, we explore the merits of using solution x-ray scattering data to estimate the imaging parameters necessary to make corrections to the structure factor amplitudes derived from electron cryomicroscopic images of icosahedral virus particles. Using 400-kV spot-scan images of the bacteriophage P22 procapsid, we have calculated an amplitude contrast of 8.0 ± 5.2%. The amplitude decay parameter has been estimated to be 523 ± 188 Å$^2$ with image noise compensation and 44 ± 66 Å$^2$ without it. These results can also be used to estimate the minimum number of virus particles needed for reconstruction at different resolutions.

## INTRODUCTION

Three-dimensional structural studies of icosahedral virus particles using electron cryomicroscopy provide a broad range of information concerning the mechanisms undertaken by this class of macromolecular complexes for biological processes such as morphogenesis, virus-cell interactions, and antibody neutralization (Baker and Johnson, 1997; Chiu et al., 1997). A distinct advantage of this electron imaging technique is the ability to retrieve both structure factor amplitudes and phases directly from the images. All electron images, however, have inherent aberrations due to the electromagnetic lenses and other instrumental factors (Brink and Chiu, 1991; Erickson and Klug, 1970). These factors affect the structure factor amplitudes and phases, resulting in decreased accuracy in the determined three-dimensional reconstruction. In the case of two-dimensional crystals, the true structure factor amplitudes are obtained from the intensities of electron diffraction patterns, which are insensitive to the image effects (Henderson et al., 1986; Unwin and Henderson, 1975). Unfortunately, in the case of spherical virus particles it is experimentally difficult to obtain electron diffraction patterns. Consequently, the true structure factor amplitudes must be determined through an alternative mechanism.

In contrast to electron imaging, solution x-ray scattering provides absolute and accurate measurement of the structure factor amplitudes of virus particles in solution (Harrison, 1969; Jack and Harrison, 1975). An x-ray scattering curve, however, provides no information on the structure factor phases. Solution x-ray scattering data have previously been used to scale the Fourier amplitudes computed from electron cryomicroscopy image data for both the acrosomal process (Schmid et al., 1991) and flagellar filaments (Mimori et al., 1995). These comparisons, however, did not estimate the values of the imaging parameters. Given the apparent complementarity between these two structural techniques, we explore the merits of combining the information provided by solution x-ray scattering and electron cryomicroscopy to obtain accurate electron cryomicroscopy amplitudes for three-dimensional reconstruction.

Images acquired in the electron microscope are degraded by the contrast transfer function (Erickson and Klug, 1970), a number of envelope decay functions (Brink and Chiu, 1991; Frank, 1976; Hanszen and Trepte, 1971), and noise (Glaeser and Downing, 1992). The effects of these functions on the images can be approximated as follows:

$$F_{\text{obs}}(S) = F(S)CTF(S)E(S) + \text{Noise}(S) \qquad (1)$$

where $F_{\text{obs}}$ are the structure factors computed from the electron cryomicroscopy images, $F$ are the true structure factors of the object under study, *CTF* is the contrast transfer function, $E$ is the product of all envelope decay functions, *Noise* is the noise function, and $S$ represents spatial frequency (reciprocal of resolution). Depending on the severity of the image degradations and the desired resolution, reconstructions obtained without correcting for the contrast transfer and/or the envelope decay functions may have inaccurate mass distributions, inaccurate internal features,

*Received for publication 10 August 1998 and in final form 1 January 1999.*

Dr. Greene's current address: G. W. Hooper Foundation, University of California San Francisco, San Francisco, CA 94143-0552.

Address reprint requests to Wah Chiu, Verna and Marrs McLean Department of Biochemistry, Baylor College of Medicine, One Baylor Plaza, Houston, TX 77030. Tel.: 713-798-6985; Fax: 713-796-9438; E-mail: wah@bcm.tmc.edu.



0006-3495/99/04/2249/13 $2.00

and inaccurate molecule boundaries (Avila-Sakar and Chiu, 1996; Jeng et al., 1989; Mimori et al., 1995; Shaw et al., 1993; Unwin, 1993). Consequently, accurate determination of the three-dimensional structure requires correction for the effects of contrast transfer and envelope decay function on the electron cryomicroscopy structure factors. These corrections are especially important at low and high resolutions, where these imaging effects are most pronounced.

We have collected solution x-ray scattering intensity data of bacteriophage P22 scaffolding-containing procapsids and infectious phage particles. After analyzing the solution x-ray scattering data and performing data fitting between the solution x-ray scattering and electron cryomicroscopy intensities, we have determined the actual contrast transfer, envelope decay, and noise functions present in the electron cryomicroscopy images. Specifically, we used the solution x-ray scattering data as the true structure factor amplitudes, *F(S),* and performed data fitting to calculate the unknown parameters, which define the contrast transfer and envelope decay functions. These determined imaging parameters allow for accurate correction of the structure factor amplitudes necessary in the determination of high resolution icosahedral virus structures using electron cryomicroscopy.

## MATERIALS AND METHODS

### Capsid preparation

P22 scaffolding mutant procapsids were prepared essentially as described previously (Prevelige et al., 1988; Thuman-Commike et al., 1996). *Salmonella typhymurium* (strain DB7136) was infected with P22 phage carrying the mutation 2*am*H202, which prevents DNA packaging. The strain used for production of the scaffolding-containing procapsid carried the mutation 8*ts*L177I, which impairs scaffolding release (Greene and King, 1996), the mutation $c_1$7, which ensures entry into the lytic pathway, and the mutation 13*am*H101, which delays lysis. Salmonella cells infected at a multiplicity of infection of 0.1 phage/cell were grown for 4 h at 30°C. Cells were harvested by centrifugation, lysed by repeated freeze/thaw cycles, and treated with DNase and RNase, after which cell debris was removed by low-speed centrifugation. The procapsids were concentrated from the supernatant by centrifugation at 45,000 rpm for 1 h in a 45Ti rotor. The procapsids were further purified by chromatography on an S-100 column, which removes membrane vesicles. Fractions containing procapsids were identified by sodium dodecyl sulfate-polyacrylamide gel electrophoresis, pooled, and concentrated by centrifugation.

Infectious phages were prepared as for procapsids, except that the infecting phage strain did not carry the 2*am*H202 mutation and thus could produce infectious phages. After the S-100 column chromatography, the infectious phage preparation was loaded onto 15-ml 15–30% sucrose gradients and centrifuged for 4.5 h at 24,000 rpm in an SW27.1 rotor. This step separates the heavier, DNA-containing infectious phages from both procapsids and unstable phage particles that have lost their DNA. The infectious phage band was removed through a pinhole at the bottom of the tube with a syringe. The sample was dialyzed to remove the sucrose and concentrated. The number of infectious phages per milliliter was determined by titering on *Salmonella typhimurium* under permissive conditions using standard procedures (Ausubel et al., 1995). The weight concentration was calculated from the number of infectious phage/ml using an estimated molecular weight of $48 \times 10^6$ daltons for the combined weight of protein and DNA in the virion.

### Solution x-ray scattering

Solution x-ray scattering experiments were conducted at Beam Line 4–2 of the Stanford Synchrotron Radiation Laboratory using a significantly upgraded version of the Biotechnology Resources small angle scattering/Diffraction instrument (Tsuruta et al., 1998). The wiggler synchrotron radiation beams were focused with a bent cylinder mirror and monochromated with a double-crystal Si(111) monochromator. The beam energy was calibrated to 8333 eV (wavelength 1.488 Å) at the NiK absorption edge. The linear position-sensitive proportional counter, BioLogic model 210 (Grenoble, France), was filled with $Xe/CO_2$ (Gabriel, 1977; Gabriel et al., 1978) and used a set of fast encoding electronics modules (Boulin et al., 1988). The sample-to-detector distance was determined using the (100) diffraction peak from cholesterol myristate powder.

Samples of P22 particles at concentrations between 20–50 mg/ml were contained in polycarbonate sample cells equipped with 25-micron-thick mica windows and maintained at a constant temperature ($20 \pm 1$°C) during data collection. The total exposure time for each sample ranged from 10 to 20 min, subdivided into 5 to 15 separate measurements of solution scattering in order to inspect for any radiation-induced time-dependent change in particle solution scattering. The detector count rate of the entire active detector area was maintained below 30,000 counts per second so that the detector counting efficiency remained virtually constant (above 98%) throughout the measurements. This was done to eliminate the risk of improper background subtraction, which could result from errors in the detector's dead time correction of the data recorded at higher count rates in the range of the inverse of the detection system dead time (1.5 ms). Blank buffer solution scattering was measured under conditions identical to the corresponding capsid particle solution scattering, normalized to integrated primary beam intensity, and subtracted from the particle solution scattering (Müller, 1982). No sample absorption correction was made because x-ray absorption of concentrated capsid solutions was essentially identical to that of the corresponding buffer solutions. All scattering curves for a given sample were corrected for detector channel response and averaged after confirming that radiation-induced changes were not present.

### Electron cryomicroscopy

Capsid samples were applied to copper grids covered with holey carbon film. Excess solution was removed by blotting and the grids were rapidly plunged into liquid ethane (Adrian et al., 1984; Dubochet et al., 1988). Samples of the P22 scaffolding-containing procapsid were kept at −168°C and imaged at a magnification of 30,000 on a JEOL 4000 electron microscope using 400-kV electrons and spot-scan imaging (Zhou et al., 1994). All images were recorded on Kodak SO-163 film. The film was developed in full-strength Kodak D19 for 12 min at 20°C, followed by fixation for 10 min in Kodak fixer.

### Image processing

Micrographs of the scaffolding-containing procapsid were scanned using a Perkin-Elmer 1010M microdensitometer (Orbital Science, Pomona, CA) at step sizes of either 10 or 17 $\mu$m. Particles were selected using automated reference-based particle selection (Thuman-Commike and Chiu, 1995, 1996). Image quality and defocus were estimated using the average sum of the Fourier transform intensities of particle images from the same micrograph (Zhou et al., 1996). In addition to particle images, small regions of the background ice ranging in size from $100 \times 100$ to $200 \times 200$ pixels were also selected from each micrograph for use in determining the noise present in the micrographs.

For comparison with the solution x-ray scattering intensity profiles, the average intensity of the Fourier transform of the electron cryomicroscopy image data as a function of spatial frequency, known as the power spectrum, was computed. For each data set, between 137 and 200 particle image Fourier transforms were summed to compute the power spectrum. Calculation of the power spectrum began by padding the particle images in real space into a larger array by adding a number of pixels to each side of the

image. The pad sizes were chosen such that the resulting step size in Fourier space closely matched the 1/3424.65 $Å^{-1}$/point step size of the collected low-angle solution x-ray scattering data. The images scanned at 17 $\mu$m were padded to 600 × 600 pixels, resulting in a Fourier space step size of 1/3464.68 $Å^{-1}$/pixel. The images scanned at 10 $\mu$m were padded to 1024 × 1024 pixels, resulting in a Fourier space step size of 1/3478.53 $Å^{-1}$/pixel. Next, the intensities of the Fourier transforms of the individual padded particle images were summed and rotationally averaged at 1° intervals. Last, the average intensity of the electron cryomicroscopy data as a function of spatial frequency was extracted from the rotationally averaged spectrum. This procedure was performed for both the particle and the ice background images of each micrograph.

## Data fitting

The unknown imaging parameters that modify the electron cryomicroscopy data were determined by fitting the electron cryomicroscopy data to the x-ray data modulated by the contrast transfer and envelope decay functions. In the data fitting we performed, the contrast transfer function (Erickson and Klug, 1970) is defined as

$$\mathrm{CTF}(S) = -(1 - Q^2)\sin(\gamma(S)) + Q\cos(\gamma(S)), \quad (2)$$

$$\gamma(S) = \pi((-C_s\lambda^3 S^4)/2 + \Delta z \lambda S^2) \quad (3)$$

where $S$ is spatial frequency, $Q$ is the fraction of amplitude contrast, $C_s$ is the spherical aberration coefficient of the objective lens, $\lambda$ is the wavelength, and $\Delta z$ is the image defocus. Note that in a given set of experiments, the wavelength and spherical aberration coefficient are fixed constants of the electron microscope and the defocus is an experimental variable, varying in different images and amplitude contrast as a function of both the specimen thickness and the composition of the given electron microscope. Using this definition, the modifications applied to the electron cryomicroscopy images relative to the solution x-ray scattering data can be expressed (Erickson and Klug, 1970, Glaeser and Downing, 1992) as

$$F_e(S) = kI_x(S)^{1/2}\,\mathrm{CTF}(S)e^{-BS^2} + N(S) \quad (4)$$

where $F_e$ is the circularly averaged amplitudes of the Fourier transform of the electron cryomicroscopy particle images (henceforth referred to as the electron cryomicroscopy amplitudes), $I_x$ is the solution x-ray scattering intensity profile (henceforth referred to as the x-ray intensities), $N$ is the circularly averaged amplitude of the noise present in the electron cryomicroscopy images calculated from the surrounding image background, $e^{-BS^2}$ is the cumulative envelope function (Glaeser and Downing, 1992; Henderson, 1992), $B$ is the amplitude decay parameter (Glaeser and Downing, 1992), and k is a scaling constant. Note that the decay parameter, $B$, has the same effect as the temperature factor used in x-ray crystallography to smear out the high-resolution data. However, the physical origins of the electron cryomicroscopy decay parameter are quite different from those of the x-ray crystallography temperature factor. The amount of electron cryomicroscopy decay can vary from image to image and is a function of the instrument, imaging conditions, and specimen stability during illumination.

We fitted $F_e(S)^2$ to $I_x(S)$ as a function of $S$ by determining the appropriate values for the unknown variables $\Delta z$, $B$, and $Q$. We should point out that although x-rays and electrons interact with matter differently, these differences are not significant until approaching 4 Å resolution (Henderson, 1995). Thus, in our fitting process we assumed that x-ray and electron scattering are the same. The defocus value was estimated by locating the positions of the contrast transfer function zeros in the image power spectrum, assuming 0% amplitude contrast (Zhou et al., 1996). Although the exact defocus will change with different amounts of amplitude contrast (Erickson and Klug, 1970), this change is not significant at the resolution ranges used in our comparisons. Thus, we have not recalculated the defocus for the determined amount of amplitude contrast. Initial values for the amplitude contrast and amplitude decay parameters were obtained by manual fitting of Eq. 4. After this initial estimation for the values of the amplitude contrast and amplitude decay parameters, a more accurate fit was performed using nonlinear least squares (Marquardt, 1963; Press et al., 1994). In the nonlinear least-squares fitting process, multiple initial starting points were used to obtain a range of values for the amplitude contrast and amplitude decay parameters. Based on the initial manual fitting we used $B$ values ranging from 0 to 1000 and $Q$ values ranging from 0 to 2%. The final results shown are the mean and standard deviations computed from the resulting nonlinear least-squares fits. Because of the large decay of $F_e(S)^2$ relative to $I_x(S)$ we performed the nonlinear least-squares fitting on the logarithm of Eq. 4. This fitting was performed both with and without the noise term in Eq. 4. In the case of background noise subtraction, the noise term, $N(S)$, was scaled to overlap the locations of the contrast transfer function zeros in $F_e(S)$.

# RESULTS

## Electron cryomicroscopy

Electron cryomicroscopy was performed on scaffolding-containing bacteriophage P22 procapsids under a variety of imaging conditions (Fig. 1 *A*). The average power spectrum computed from the selected particle images in each of these micrographs provides a visual mechanism for identifying the location of the contrast transfer function zeros, a quantitative mechanism for assessing the quality of the images (Zhou et al., 1996), and a mechanism for visualizing the particles' characteristic circularly averaged structure factors. Fig. 1, *B* and *C*, shows the computed average power spectrum and corresponding circularly averaged plot for the micrograph shown in Fig. 1 *A*. Notice that in this power spectrum three contrast transfer function zeros are visible, as highlighted by the arcs (Fig. 1 *B*). The locations of these contrast transfer function zeros at 1/24, 1/17, and 1/14 $Å^{-1}$ indicate an image defocus of 3.45 $\mu$m underfocus. Furthermore, the location of the last visible contrast transfer function zero, which in this example is 1/14 $Å^{-1}$, suggests the image may contain structural data out to this resolution. In addition to these image quality features, the average power spectrum provides a visualization mechanism for the structure factor peaks of the virus under study. In Fig. 1, *B* and *C*, the most readily visible structure factor peaks lie between 1/200 and 1/32 $Å^{-1}$. These low resolution peaks (Fig. 1 *B, arrow*) correspond to the scattering function of the icosahedral particles (Jack et al., 1975). Visualization of these structure factor peaks beyond 1/32 $Å^{-1}$ is hindered by the presence of noise, the contrast transfer function zeros, and the envelope decay present in the images.

## Solution x-ray scattering

Bacteriophage P22 scaffolding-containing procapsids and infectious phages were purified and prepared for solution x-ray scattering. Two sample-to-detector distances were used for the data collection. Specifically, a 129-cm camera covered the resolution range of 1/214–1/13.5 $Å^{-1}$ and a 30-cm camera covered the resolution range of 1/66–1/4.34 $Å^{-1}$. Shown in Fig. 2 are plots of the resulting solution x-ray scattering intensities for both the low- and high-angle camera settings. Statistical analysis of the features in these x-ray scattering intensity profiles indicates that all observed

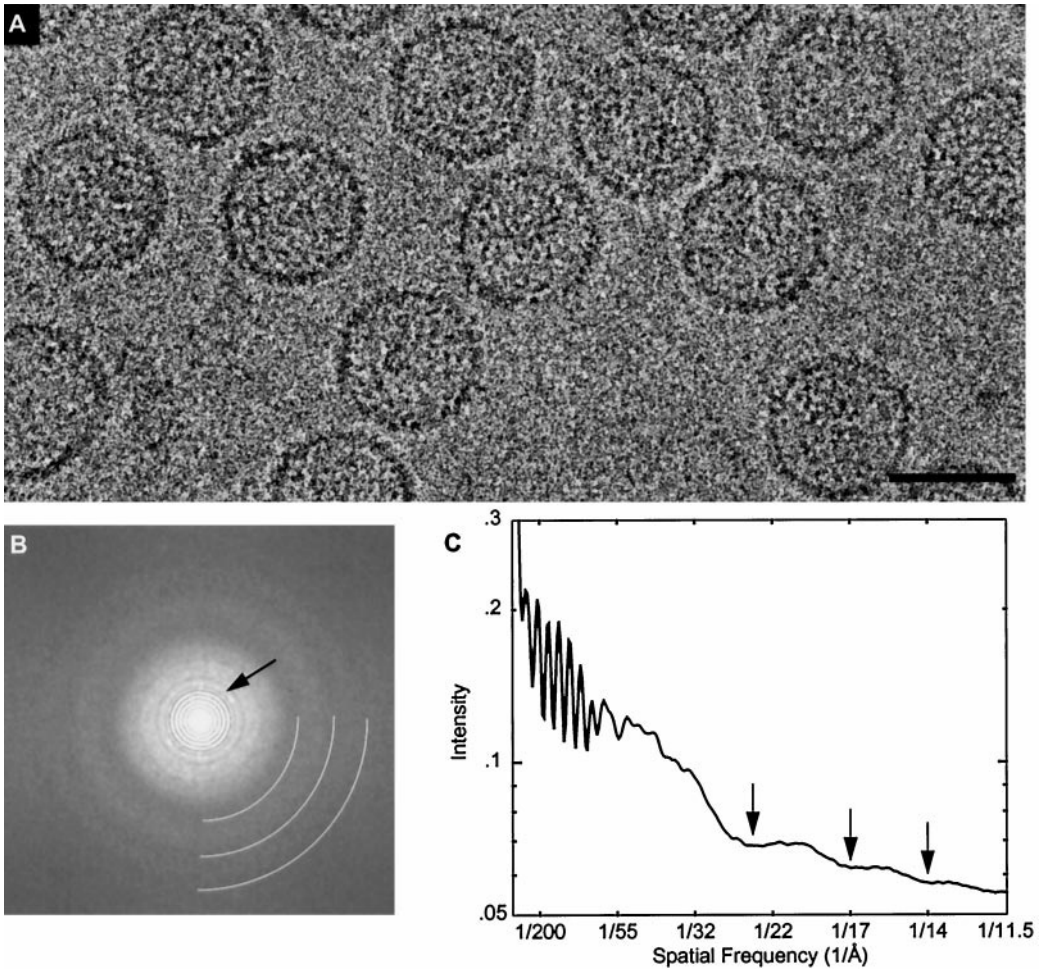


FIGURE 1 Electron cryomicroscopy images and computed average power spectrum. (*A*) Selected region from a 3.45-$\mu$m underfocus electron cryomicroscopy image of the bacteriophage P22 scaffolding-containing procapsid. Scale bar, 500 Å. (*B*) Average power spectrum computed from 137 particle images present in the micrograph shown in *A*. The white arcs denote the locations of the contrast transfer function zeros in the power spectrum and the black arrow denotes the low-resolution structure factors. (*C*) Circularly averaged plot of the average power spectrum shown in *B*. The arrows correspond to the locations of the contrast transfer function zeros denoted by the white arcs in *B*.

features are significant within the stated resolution ranges. Consequently, the overall decay of the observed x-ray scattering data is interpretable. In the case of the features at high resolution, however, the significance of the individual peaks is less than the significance of the large peaks present at low resolution.

In the case of the low-angle camera setting, the profile for the infectious phage (Fig. 2 *A*, *light line*) is similar to the scaffolding-containing procapsid profile (Fig. 2 *A*, *bold line*) except that the location of the structure factor peaks below 1/50 $Å^{-1}$ is shifted to the left. This shift corresponds to the enlargement the capsid undergoes during DNA packaging (Prasad et al., 1993). At higher resolution, the infectious phage profile (Fig. 2 *A*, *light line*) contains a large peak at 1/24 $Å^{-1}$ corresponding to the internal DNA, as previously described (Earnshaw et al., 1976).

In addition to this moderate resolution solution x-ray scattering profile, we obtained a high-angle profile extending to 4.34 Å resolution (Fig. 2 *B*) for scaffolding-containing procapsids and infectious phages. Both of these profiles contain many strong features up to $\sim$1/9 $Å^{-1}$, at which point a substantial decay occurs. After this decay, the intensities for the scaffolding-containing procapsid increase in intensity beginning at 1/6 $Å^{-1}$, resulting in a broad peak with a maximum located $\sim$1/4.6 $Å^{-1}$.

## Comparison of solution x-ray scattering and electron cryomicroscopy intensities

Comparison of the x-ray intensities and the squared electron cryomicroscopy amplitudes (intensities) is exemplified in Fig. 3. The most striking feature of this comparison is that the relative decay between the two curves differs by three orders of magnitude (Fig. 3 *A*). This difference in the magnitude of decay between the electron cryomicroscopy and solution x-ray scattering data emphasizes the large extent to which the electron cryomicroscopy amplitudes have been modified during imaging. Comparison of the electron cryomicroscopy and x-ray intensities up to 1/50

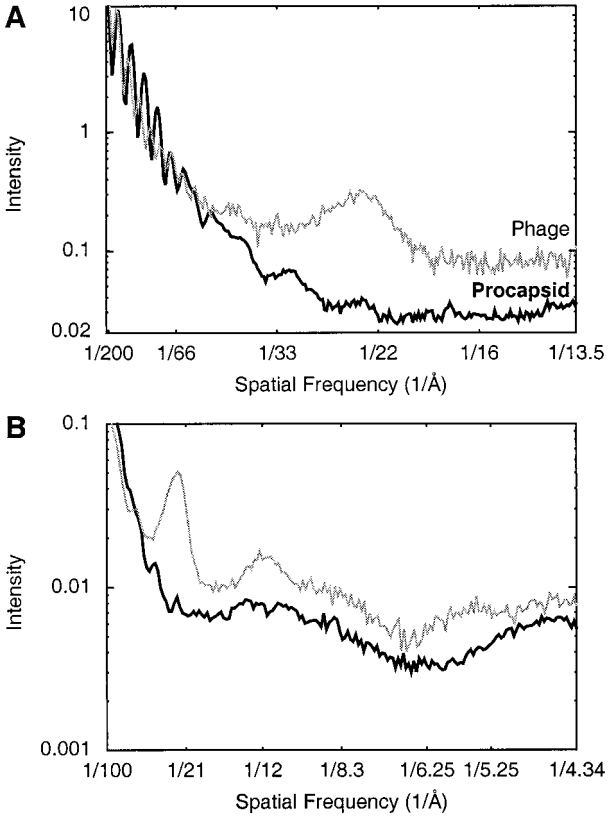


FIGURE 2 Plot of solution x-ray scattering intensities for the scaffolding-containing procapsid (*bold line*) and the mature phage (*light line*). (*A*) Low-angle data sets in the resolution range of 1/214–1/13.5 $Å^{-1}$. The intensities of the plots have been aligned at the 1/152 $Å^{-1}$ peak for comparison. (*B*) High-angle data set in the range 1/66–1/4.34 $Å^{-1}$ aligned at the 1/42 $Å^{-1}$ peak for comparison.

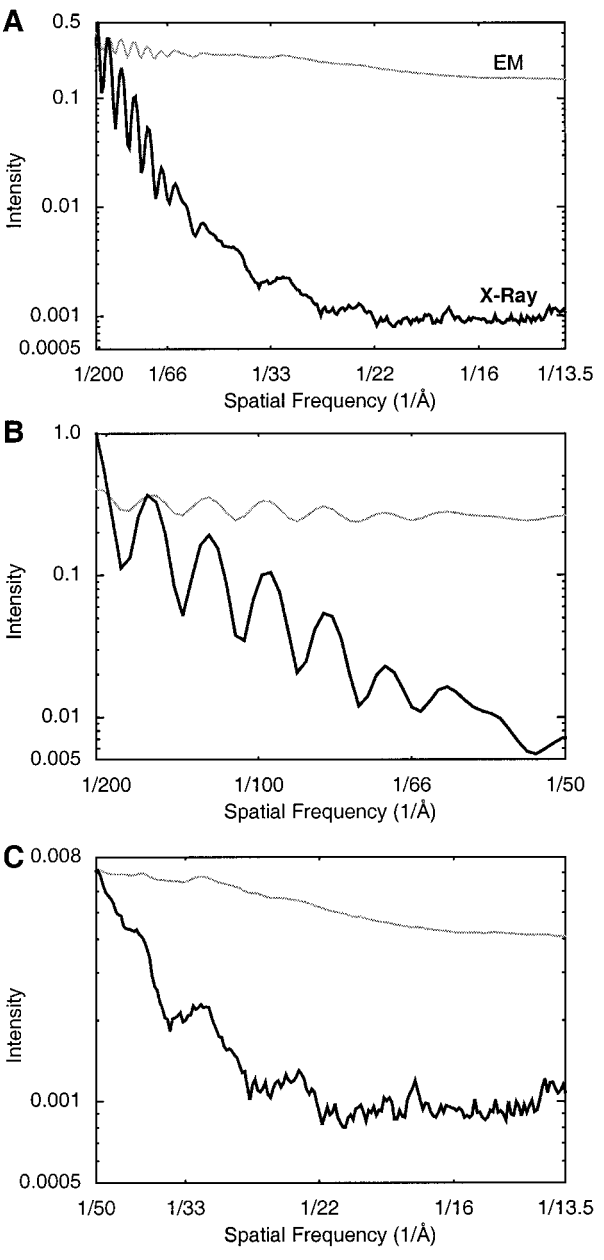


FIGURE 3 Comparison of circularly averaged electron cryomicroscopy and solution x-ray scattering intensities of scaffolding-containing procapsids. The light line shows the electron cryomicroscopy intensities for a 400-kV spot-scan micrograph at 1.75 $\mu$m underfocus. The bold line corresponds to the x-ray intensities obtained at the low-angle camera setting. (*A*) Plot of the data in the range 1/214–1/13.5 $Å^{-1}$ aligned at the 1/152 $Å^{-1}$ peak. (*B*) Plot of the data in the range of 1/214–1/50 $Å^{-1}$ aligned at the 1/152 $Å^{-1}$ peak. (*C*) Plot of the data in the range of 1/50–1/13.5 $Å^{-1}$ aligned at the 1/50 $Å^{-1}$ peak.

$Å^{-1}$ demonstrates the consistent placement of structure factor peaks between these two data collection techniques (Fig. 3 *B*). It should be pointed out that the x-ray scattering intensity was measured from a solution sample containing $\sim 10^8$ virus particles, whereas the electron cryomicroscopy intensities were computed from images of fewer than 200 particles. Further notice that although these peaks align out to 1/13.5 $Å^{-1}$ (Fig. 3 *C*), because of the noise, contrast transfer, and envelope decay functions, the strength of the electron cryomicroscopy peaks beyond 1/50 $Å^{-1}$ is severely weakened. Consequently, visualization of structure factor peak alignment beyond 1/50 $Å^{-1}$ is hindered.

Electron cryomicroscopy data are modified by the contrast transfer and envelope decay functions characterized by three parameters: defocus, percent of amplitude contrast, and amount of envelope decay. In addition, electron cryomicroscopy data are corrupted by a significant amount of noise that is contributed by the presence of background materials and scattering statistical fluctuations (Glaeser and Downing, 1992). Given the complexity of these independent functions, we have employed a stepwise process to fit the electron cryomicroscopy data to the solution x-ray scattering data and subsequently determine the unknown imaging parameters. First, we determined the image defocus by analyzing the average power spectrum of the individual electron cryomicroscopy particle images (Zhou et al., 1996). Next, we performed a manual fitting of the electron cryomicroscopy and solution x-ray scattering intensities to determine initial values for amplitude contrast and envelope decay. Using these initial values as starting points, we then performed nonlinear least-squares data fitting for each electron

micrograph. These data fittings were performed both with and without compensation for the electron cryomicroscopy noise function as described below. The results we present are the mean and standard deviation of the values determined by the various nonlinear least-squares data fitting operations.

### Structure factor fitting without noise compensation

We began our nonlinear least-squares data fitting without compensating for the electron cryomicroscopy noise function. Fig. 4 shows the resulting fit between the electron cryomicroscopy and x-ray intensities with the plotted values of $B$ and $Q$ chosen for a consistent, visually appealing representation of the displayed plots. The chosen fit is within the mean of all possible fits and we opted for the one matched with most of the peaks for the chosen figures. In these curves, the consistency of the structure factor peaks between the two data sets is readily apparent. Furthermore, examination of the accuracy of the match between the electron cryomicroscopy and x-ray intensities after correction shows that the relative decay between the two intensity profiles is consistent except in the regions surrounding the contrast transfer function zeros, where the electron cryomi-

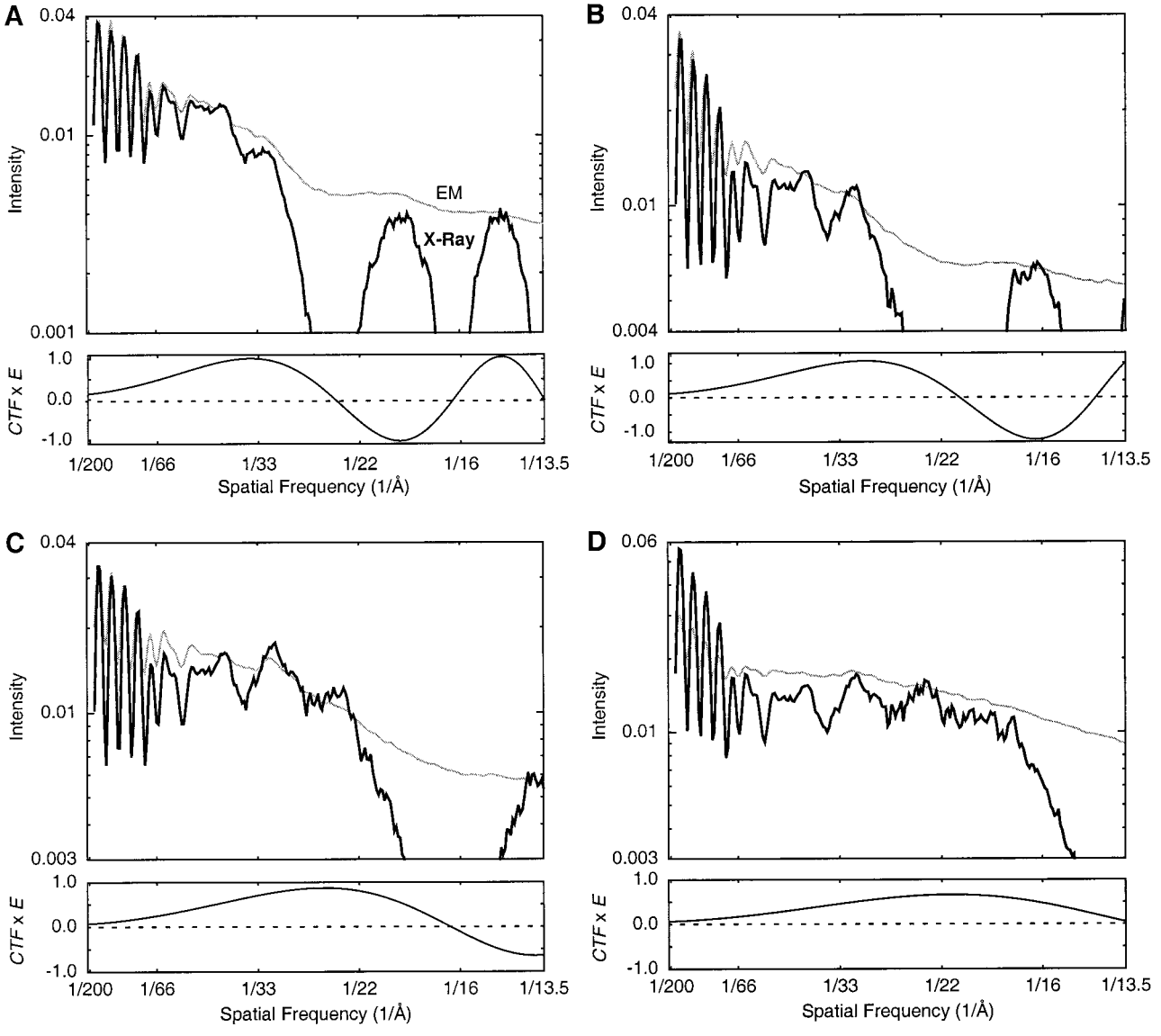


FIGURE 4 Comparison of solution x-ray scattering and electron cryomicroscopy intensities of scaffolding-containing procapsids after correction for the contrast transfer and envelope decay functions without noise compensation. In each panel, the upper plot compares the x-ray intensities modified by the contrast transfer and envelope decay functions (*bold line*) to the electron cryomicroscopy intensities (*light line*). In the lower plot of each panel, the corresponding image degradation function is depicted by the product of the contrast transfer and envelope decay functions. The data are shown in the range of 1/214–1/13.5 $Å^{-1}$. The plots correspond to the different micrographs of the scaffolding-containing procapsid as follows: *A,* 3.45 $\mu$m; *B,* 2.60 $\mu$m; *C,* 1.75 $\mu$m; *D,* 1.10 $\mu$m underfocus. The average percentage of amplitude contrast is 8.8 $\pm$ 3.6% and the average amplitude decay is 44 $\pm$ 66 $Å^2$ from this set of data.

croscopy datum does not become zero because noise compensation has not been performed. That is, these regions of dissimilarity occur because the background noise has not been subtracted from the electron cryomicroscopy intensities. Despite the absence of noise function correction, however, the fit between these curves is quite good. Furthermore, the presence of the contrast transfer function zeros substantiates the fitting process by demonstrating the consistency between the processed data sets and the inconsistency that occurs because of failure to correct for the noise present in the electron cryomicroscopy images.

### Structure factor fitting with noise compensation

In order to account for the decay at the contrast transfer function zeros the electron cryomicroscopy noise function was included in the nonlinear least-squares data fitting. The exact nature of the noise present in electron cryomicroscopy images is currently unknown. However, several models have been proposed that characterize the additive noise using exponential functions (Glaeser and Downing, 1992; Perkins et al., 1995; Zhu et al., 1997). Unfortunately, these noise models introduce several additional unknown parameters into the data fitting. Given the complexity of the functions we were fitting, the use of additional parameters severely weakens the ability to determine a unique set of unknown parameters that will match the electron cryomicroscopy data to the solution x-ray scattering data. Consequently, we chose to simplify the data fitting by using the amplitude profile of the electron cryomicroscopy image of ice as a background to represent the noise function. That is, when performing data fitting with noise compensation, we subtract the noise amplitude profile from the electron cryomicroscopy amplitudes before performing the nonlinear least-squares fit.

The resulting fit between the electron cryomicroscopy intensities after subtracting noise and the modified x-ray intensities is shown in Fig. 5 along with the determined imaging parameters. As with the previous comparison (Fig. 4), the consistency of the structure factor peaks between the two data sets is apparent. In the case of the far-from-focus images the determined amount of envelope decay severely weakens the strength of the electron cryomicroscopy data (Fig. 5, *A* and *B*, contrast transfer function plot). Thus, the apparent mismatch in the electron cryomicroscopy and x-ray intensities beyond the location of the first contrast transfer function zero for both far-from-focus images is a result of the extremely small value of the applied image degradation functions. We interpret these results as indicating that the electron cryomicroscopy data in the far-from-focus images are valid only up to the locations of the first contrast transfer function zeros. That is, beyond the first contrast transfer function zero the signal is dominated by noise. In the close-to-focus images (Fig. 5, *C* and *D*) a similar effect is not observed. Thus, the close-to-focus electron cryomicroscopy data are valid in the entire range plotted. Examination of the curves corresponding to the close-to-focus images shows that upon the additional compensation for noise, the relative decay between the electron cryomicroscopy and x-ray intensity curves is consistent up to, including, and beyond the locations of the contrast transfer function zeros. That is, in the data-fitting comparison with noise compensation, the region of dissimilarity surrounding the contrast transfer function zeros is smaller than those in the comparisons without noise compensation.

### Calculation of amplitude contrast *Q* and amplitude decay *B*

The calculated percentage of amplitude contrast in the noise-compensated comparisons is $8.0 \pm 5.2\%$. In comparison, the calculated percentage of amplitude contrast without noise compensation is $8.8 \pm 3.6\%$. Thus, compensating for noise during data fitting resulted in only a relatively minor change in the percentage of amplitude contrast. We would expect such a result because the main effect of amplitude contrast is at low resolution, whereas the main effect of noise is at high resolution. Thus, compensation for noise should not produce a vastly different result at low resolution. Note, however, that our chosen noise compensation method could result in inaccuracies in the determined percentage of amplitude contrast due to the possible presence of contaminants, such as proteins, in the background image. Although this may account for the large standard deviation in the noise-compensated comparisons, comparison of our results with and without noise compensation argues against this affecting our overall results because the calculated mean percent of amplitude contrast does not significantly change in either data fitting method.

In the case of the determined amount of amplitude decay, a significantly large change in value occurs upon compensation for the noise function. Specifically, without noise compensation, the amount of amplitude decay is $44 \pm 66$ Å$^2$ but upon noise compensation this value rises to $524 \pm 188$ Å$^2$. This significant change is expected because the principal effect of the additive noise is at high resolution. Thus, comparison of the calculated values before and after noise compensation is consistent to each other and further substantiates the utility of this method.

Because the determined amount of amplitude decay differs greatly when computed with and without noise compensation, it is clear that the choice of noise function greatly affects the amount of amplitude decay. Given that the noise function is calculated from the background image and is not a known or directly computable function, it is possible that our chosen noise function does not accurately account for the actual noise present in the images. It may be that the moderately large standard deviations in our amplitude decay function calculations are a result of these possible inaccuracies. In this case, the actual amount of amplitude decay may lie between the values we have determined with noise compensation and those determined without it. It should be noted, however, that the calculated amount of amplitude

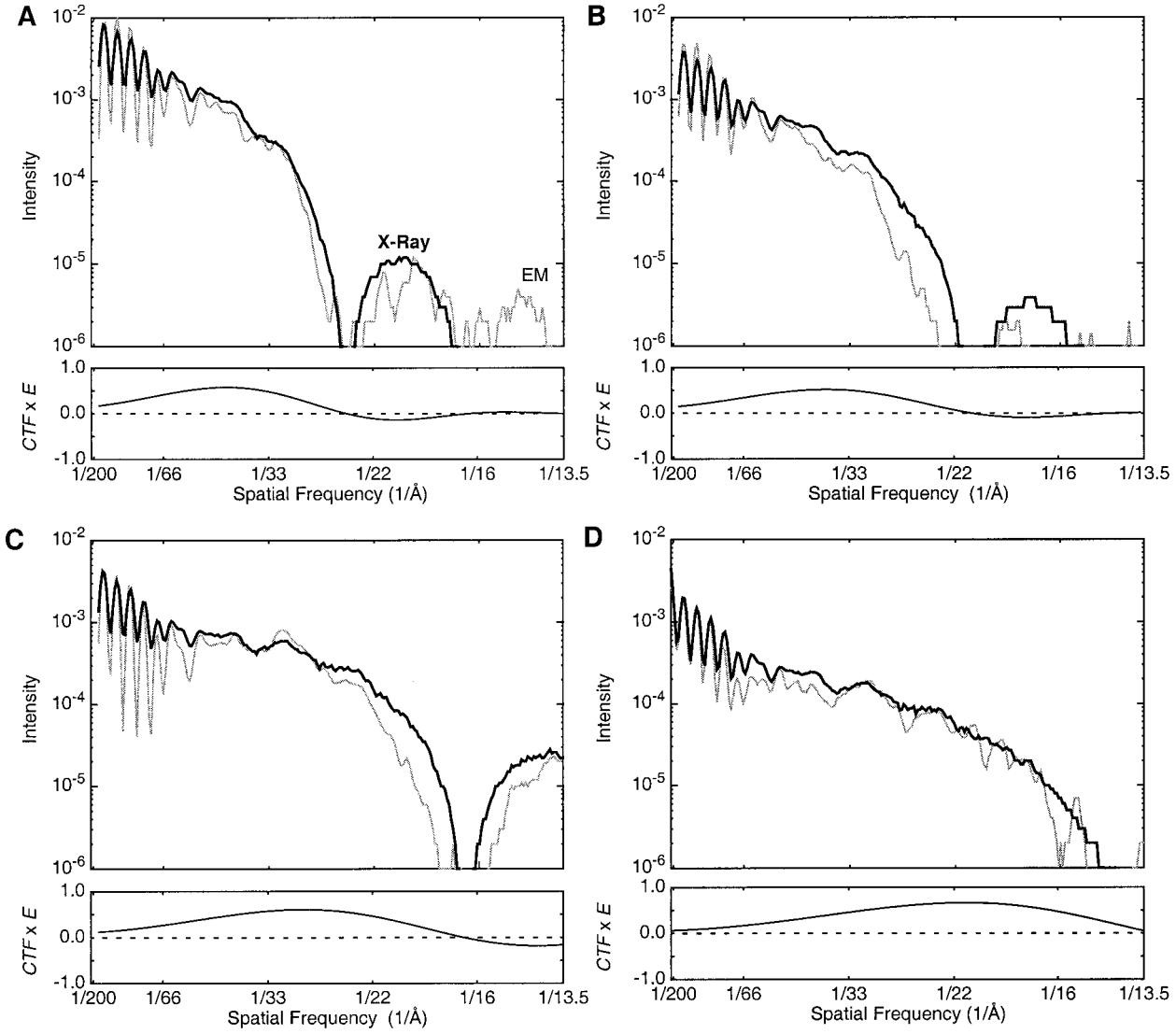


FIGURE 5 Comparison of solution x-ray scattering and electron cryomicroscopy intensities after correction for the contrast transfer, envelope decay, and noise functions. In each panel, the upper plot compares the x-ray intensities modified by the contrast transfer and envelope decay functions (*bold line*) to the electron cryomicroscopy intensities modified by the noise function (*light line*). In the lower plot of each panel, the corresponding image degradation function is depicted by the product of the contrast transfer and amplitude decay functions. The data are shown in the range of 1/214–1/13.5 $Å^{-1}$. The plots correspond to the different micrographs of the scaffolding-containing procapsid as follows: *A,* 3.45 $\mu$m; *B,* 2.60 $\mu$m; *C,* 1.75 $\mu$m; *D,* 1.10 $\mu$m underfocus. The average percent of amplitude contrast is 8.0 $\pm$ 5.2% and the average amplitude decay is 523 $\pm$ 188 $Å^2$ from this set of data.

decay is also dependent on the quality of the individual electron cryomicroscopy images, a factor that will vary from experiment to experiment and from image to image. Thus, the slightly elevated standard deviations we observed could have resulted from variations in the overall quality of our tested images.

## DISCUSSION

### Structural characteristics suggested by solution x-ray scattering

In addition to using the solution x-ray scattering data for calculation of the electron cryomicroscopy imaging factors, we have analyzed the solution x-ray scattering data for structural information on bacteriophage P22. Comparison of the infectious phage and scaffolding-containing procapsid structure factor peaks reveals that the locations of the infectious phage structure factor peaks below 1/50 $Å^{-1}$ are to the left of the procapsid structure factor peaks. This shift corresponds to the enlargement the capsid undergoes during DNA packaging (Prasad et al., 1993). In addition to this shift in the low-resolution peaks, the infectious phage profile contains several additional structure factor peaks not present in the procapsid profile. Specifically, the infectious phage profile contains additional peaks at 1/24, 1/12, 1/8.5, and 1/5.6 $Å^{-1}$. These peaks have been previously observed in P22 phage and are attributed to the internal phage DNA (Earnshaw et al., 1976). The spacing of the DNA-related

peaks, with the exception of the 1/24 $Å^{-1}$ peak, is consistent with the B form of DNA (Maniatis et al., 1974), as further supported by Raman difference spectroscopy results (Aubrey et al., 1992). The 1/24 $Å^{-1}$ DNA-related peak has been previously attributed to the specific packing of the DNA within the infectious phage (Earnshaw et al., 1976; Earnshaw and Harrison, 1977).

Excluding the peaks resulting from the DNA, additional structural information is provided by the significant peaks we observe at 1/10.5 and 1/4.6 $Å^{-1}$ in both the scaffolding-containing procapsid and the infectious phage. Structures containing a large number of either $\alpha$-helices or $\beta$-sheets produce structure factor peaks near 1/10 $Å^{-1}$. At higher resolution, however, structures containing a large number of $\alpha$-helices produce a peak near 1/5.1 $Å^{-1}$ (Astbury and Woods, 1933; Blaurock, 1975; Henderson, 1975; Pauling and Corey, 1951), whereas structures containing a large number of $\beta$-sheets produce a peak near 1/4.65 $Å^{-1}$ (Astbury and Sisson, 1935). In the case of both the bacteriophage P22 scaffolding-containing procapsid and the infectious phage, we do not observe a significant peak in the 1/5.1 $Å^{-1}$ range but we do observe a strong peak at 1/4.6 $Å^{-1}$. Thus, we interpret these results as indicating the bacteriophage P22 coat protein is predominantly folded into $\beta$-sheets. These results are consistent with previous studies using Raman spectroscopy (Prevelige et al., 1990; Thomas et al., 1982; Tuma et al., 1996).

### Amplitude contrast *Q*

An experimental procedure for determining the percentage of amplitude contrast by comparing two images of the same object at different defocus values has been previously described (Toyoshima and Unwin, 1988). Use of this method by Toyoshima and Unwin (1988) on images of flattened tubular vesicles of the nicotinic acetylcholine receptor resulted in a determination of 7% amplitude contrast. Further use of this method on tubular crystals of the acetylcholine receptor and calcium-ATPase resulted in amplitude contrast contributions of 5.8% at 120 kV and 4.8% at 200 kV (Toyoshima and Yonekura, 1993). In addition, the method of Toyoshima and Unwin (1988) has been used on images of tobacco mosaic virus, yeilding a result of 14 $\pm$ 2% amplitude contrast (Smith and Langmore, 1992). Recently a computational modeling approach has also been used to determine the percentage of amplitude contrast (Zhu et al., 1997). In this later approach, electron cryomicroscopy data are fitted to a number of functions depicting the degradations present in the electron cryomicroscopy images (Zhu et al., 1997). Use of this modeling method on images of the 70S ribosome subunit resulted in determination of 14% amplitude contrast in energy-filtered images and 9% in images without energy filtration (Zhu et al., 1997). In comparison, our experiments on the bacteriophage P22 procapsid determined 8.0 $\pm$ 5.2% amplitude contrast.

Amplitude contrast depends on the average atomic mass of the sample (Erickson and Klug, 1970) and inelastic scattering (Erickson, 1973). In the cases of tobacco mosaic virus (Smith and Langmore, 1992) and the 70S ribosome (Zhu et al., 1997), both samples contain nucleic acids and both sets of imaging conditions exclude inelastic scattering through energy filtration. Thus, these factors may account for the higher determined values of amplitude contrast. In the cases of the acetylcholine receptor and calcium-ATPase (Toyoshima and Unwin, 1988; Toyoshima and Yonekura, 1993), however, the samples do not contain any atoms with high atomic mass and during image formation inelastically scattered electrons are included. Thus, these two factors may account for the lower determined values of amplitude contrast for these samples. Our results for the P22 procapsid, which does not contain any nucleic acids or high atomic mass atoms, are consistent with those for other samples that do not contain nucleic acids. In addition, our images with 400-kV electrons would have less inelastic scattering than those of 100-kV images for the same irradiating electron dosage.

### Amplitude decay *B*

The envelope decay function has been attributed to a number of effects including partial spatial coherence (Frank, 1973; Frank, 1975; Wade and Frank, 1977), temporal coherence (Frank, 1976), recording medium contrast modulation (Downing and Grano, 1982; Sherman et al., 1996), inelastic scattering (Glaeser, 1982), radiation damage (Glaeser, 1971; Jeng et al., 1984), beam-induced specimen movement (Bullough and Tulloch, 1990; Downing, 1991; Henderson and Glaeser, 1985), specimen charging (Jakubowski et al., 1989), and specimen cryo-holder instability (Downing and Chiu, 1990). Each of these factors has its own envelope function. In addition, the overall decay factor may be affected by the statistical definition of the electron microscopy intensities computed from the limited number of particles present in a single electron cryomicroscopy image. These various factors can be approximated as a product of the different envelope functions (Frank, 1976; Hanszen and Trepte, 1971). We have chosen to use the $e^{-BS^2}$ approximation for the envelope decay factor. In this approximation, $B$ specifies the amount of amplitude decay.

Given the complexity of the various factors that result in the envelope decay function, no single experimental method can be performed to calculate the amount of amplitude decay. In the event that an atomic resolution model of the three-dimensional structure or some component thereof exists, computational methods may be employed to calculate the amount of amplitude decay (Grimes et al., 1997; Stewart et al., 1993). The first such example, using the major capsid protein of adenovirus (Roberts et al., 1986), computationally determined an amplitude decay of 3000 $Å^2$ for data extending to 25 Å resolution (Stewart et al., 1991). Similar calculations were performed for the bluetongue virus core using the crystal structure of the VP7 trimer (Grimes et al., 1997). In the case of bluetongue virus, an amplitude decay

of 500 $Å^2$ was calculated for data extending to 23 Å using experimental conditions that closely match those of our test images (Grimes et al., 1997). In our experiments, we have determined, for 400-kV spot-scan images of bacteriophage P22 procapsids, an amplitude decay of 523 $\pm$ 188 $Å^2$ for data extending to 13.5 Å. Thus, our determined amount of amplitude decay closely matches the value determined by Grimes et al. (1997). In comparison, the amount of amplitude decay determined by Stewart et al. (1993) for adenovirus is roughly five times larger than both the bluetongue and P22 values. The exact cause for this discrepancy is unknown; however, spatial and temporal coherence and different experimental conditions are likely contributing factors. In addition, Stewart et al. (1993) performed noise correction, which, as shown by our results, can have a substantial effect on the determined *B* value.

## Contrast transfer and amplitude decay correction in three-dimensional structures

Correction for the contrast transfer and envelope decay functions is necessary to obtain accurate high resolution three-dimensional structures. In recent years a variety of methods have been proposed and used for such correction. The majority of these correction methods perform corrections based on specified contrast transfer and envelope decay functions. These correction methods include a number of Wiener filter derivatives that incorporate noise function correction (Böttcher and Crowther, 1996; Böttcher et al., 1997; Conway et al., 1997; Trus et al., 1997; Zhou et al., 1994; Zlotnick et al., 1996) and variant Wiener methods that do not incorporate noise function correction (Mimori et al., 1995; Unwin, 1993). The values of amplitude contrast and amplitude decay used by such correction methods will affect the three-dimensional structure. Variations in the choice of amplitude contrast affect the density distribution (Mimori et al., 1995; Shaw et al., 1993; Unwin, 1993). Similarly, variations in the choice of the amplitude decay and noise functions affect the strength of high-frequency terms, resulting in differences in molecular boundaries and accuracy of the high resolution structural features. We have demonstrated a method to calculate values for the amplitude contrast and decay parameters using solution x-ray scattering. These values provide an independent experimental basis for affirming the chosen values for the contrast transfer and envelope decay function parameters used in the correction methods. As our results indicate, the amount of amplitude decay differs significantly depending on the amount of noise correction. It is also apparent in our analysis that the noise function is difficult to determine precisely.

Correction for the image degradation functions may occur at different stages of the three-dimensional reconstruction procedure. The contrast transfer function can be applied to individual particle images before three-dimensional reconstruction (Conway et al., 1997; Trus et al., 1997; Zhou et al., 1994; Zlotnick et al., 1996) or to the reconstructions of individual micrographs that are subsequently combined (Böttcher and Crowther, 1996; Böttcher et al., 1997). In either case, the contrast transfer function is applied to data from a single micrograph, not multiple micrographs. In contrast, the envelope decay function may be applied to the data of individual micrographs or to the merged data from several micrographs. If the envelope decay function is applied to individual micrographs it is essential to ensure that the applied amount of amplitude decay is consistent with the type of noise function correction applied during contrast transfer function correction. That is, in the majority of the Wiener filter-based correction methods a noise function is incorporated into the correction. For these correction methods, the applied noise function should be the same as that used to determine the amount of amplitude decay. For alternative and variant Wiener methods that do not perform noise correction, the applied amount of amplitude decay should be that determined by data fitting without compensation for the noise function. Failure to choose the appropriate noise function and corresponding amount of amplitude decay may result in an unjustified amplification of the high-frequency terms.

Given the potential inaccuracy in measuring amplitude decay for individual micrographs and the difficulty of determining image background noise subtraction accurately, it may be more beneficial to perform overall envelope decay function correction after merging of micrographs with different defocuses (with appropriate phase flips) than to make the correction to individual micrographs. In this case, the regions surrounding the contrast transfer function zeros would be compensated for by the incorporation of data from several different defocus values, reducing the amplification of noise during envelope decay correction. In this correction method, the choice of the overall amplitude decay parameter value for correction could then be guided by computing the average of the upper and lower values determined by the method described here (Figs. 4 and 5). Furthermore, after these corrections have been applied, the computed intensities of the corrected three-dimensional map to the solution x-ray scattering data could be compared to confirm proper envelope decay parameter correction. Using a Wilson plot for this comparison would plot the natural logarithm of the electron microscopy amplitudes divided by the solution scattering amplitudes as a function of spatial frequency squared. Under this formulation, the slope of the Wilson plot equals the value of the amplitude decay parameter. Thus, calculation of the Wilson plot can easily be used to validate the amount of amplitude decay correction applied to the three-dimensional reconstruction.

## Solution x-ray scattering-based estimation of the number of images needed for three-dimensional reconstruction

Estimation of the number of images needed for three-dimensional reconstruction is useful to understand the experimental and computational scope of pursuing a high-reso-

lution structural study. Solution x-ray scattering can assist in this estimation. Specifically, the number of images needed is proportional to the structure factor intensity (Unwin and Henderson, 1975). Thus, if the minimum number of images needed to determine a structure at a particular resolution can be estimated, then examination of the decay present in the solution x-ray scattering intensity data can be used to approximate the number of individual particle images needed for a higher resolution electron cryomicroscopy structure.

Theoretically, the minimum number of images needed to determine a structure at a particular resolution, $d$, for an asymmetrical object of a specific diameter, $D$, is $\pi D/d$. In reality, many more particle images are needed than this estimate suggests, even at low resolution, due to the low contrast of the images. Thus, a method incorporating real data is needed to estimate the number of particles. One method of performing this estimation is to define the minimum number of particles as the number at which the phase residual between two independent reconstructions is no longer increased by the addition of more particles. Given this empirical estimate for the minimal number of particles needed at low resolution, examination of the decay present in the solution x-ray scattering intensity data can be used to approximate the number of individual particle images needed for a high-resolution electron cryomicroscopy structure.

For example, assume 200 particle images are sufficient for determination of a 19-Å structure of the bacteriophage P22 scaffolding-containing procapsid (Thuman-Commike et al., 1996). Examination of the solution x-ray scattering data in the range of 1/20 to 1/6.25 $Å^{-1}$ (Fig. 2 *B*) shows that the intensity decays from 0.007 to 0.0033 when $B = 0$. That is, the structure factor intensity is roughly 2 times smaller at 1/6.25 $Å^{-1}$ than at 1/20 $Å^{-1}$. Because the number of images needed is proportional to the structure factor intensity (Unwin and Henderson, 1975), a minimum of 400 particle images will be needed to determine the structure of the scaffolding-containing P22 procapsid at 6.25 Å. This estimation, however, does not include the noise or the envelope decay functions present in the electron cryomicroscopy images. As shown in Fig. 6, depending on the severity of the image decay functions, the estimated number of particles needed for structure determination at 6.25 Å could significantly increase. Specifically, choice of an amplitude decay value of 50 $Å^2$, based upon use of reconstruction methods without noise compensation, results in an intensity that is roughly 25 times smaller at 1/6.25 $Å^{-1}$ than at 1/20 $Å^{-1}$. Thus, the minimum number of particles needed for structure determination at 6.25 Å increases to 5000. In addition, the necessary number of images will depend on the homogeneity of the specimen, the accuracy of the determined particle orientations, the accuracy of the three-dimensional reconstruction algorithm, and the accuracy of the envelope decay function correction algorithm. Consequently, these estimates should be considered lower bounds for the number of particle images needed for three-dimensional reconstruction to a specified resolution. In reality, one may expect to process a minimum of 3 to 4 times more particles than this theoretical estimate, simply because not every particle is equally good.

## CONCLUSIONS

We have collected solution x-ray scattering data of bacteriophage P22 scaffolding-containing procapsids and infectious phage particles. Examination of the solution scattering data indicates a strong likelihood that the P22 coat protein (gp5) is composed primarily of $\beta$-sheet structures. We have

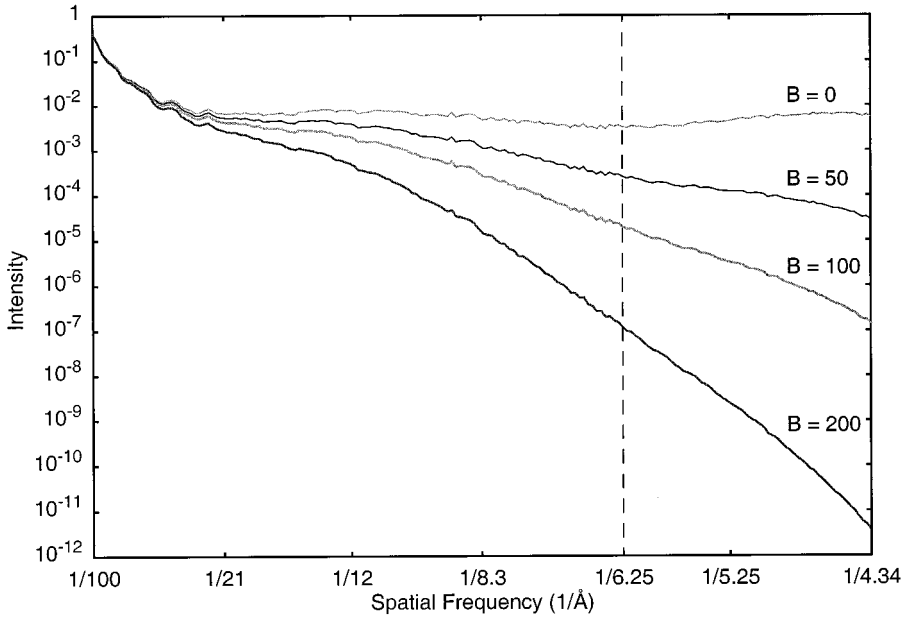


FIGURE 6 Example of the effects of the amplitude decay function. Plotted is the high-angle solution x-ray scattering intensity data of the bacteriophage P22 scaffolding-containing procapsid with an artificial amplitude decay function applied. The amount of amplitude decay applied is 0, 50, 100, and 200 $Å^2$, as indicated. The dotted vertical line corresponds to 1/6.25 $Å^{-1}$.

further used this solution scattering data to determine the unknown imaging conditions present in electron cryomicroscopy images. In our experiments using 400-kV spot-scan images of the bacteriophage P22 procapsid, we have calculated 8.0 ± 5.2% amplitude contrast and 523 ± 188 $Å^2$ or 44 ± 66 $Å^2$ amplitude decay with or without image noise compensation. These calculations are consistent with other experimental and computational methods that calculate either amplitude contrast or amplitude decay. This consistency demonstrates the ability of this method to determine the values for amplitude decay and amplitude contrast. The effects of these imaging parameters on computed reconstructions are most pronounced at high resolution. Thus, our ability to collect solution x-ray scattering data extending to 1/4.5 $Å^{-1}$ further demonstrates that upon determination of near atomic resolution electron cryomicroscopy icosahedral virus structures, the proper contrast transfer and envelope decay function parameters can be calculated and applied, allowing accurate high-resolution three-dimensional structure determination using electron cryomicroscopy.

The authors thank Drs. Michael B. Sherman and Steve Ludtke for many helpful discussions, Drs. Michael B. Sherman and Roman Tuma for comments on the manuscript, and Ms. Joanita Jakana for providing electron images of the bacteriophage P22 scaffolding-containing procapsids. Solution x-ray scattering experiments were performed at the Stanford Synchrotron Radiation Laboratory, which is funded by the Office of Basic Energy Sciences of the U.S. Department of Energy, and by grant P41RR01209 from National Institutes of Health. This research has also been supported by other grants including NIHGM17980 (to J.K.); NIHGM47980 (to P.E.P.); NIHP41RR02250, NSFBIR-9413229, NSFBIR-9412521, NIHAI38469, and Human Frontier Science RG537/96 (all to W.C.).

## REFERENCES

Adrian, M., J. Dubochet, J. Lepault, and A. W. McDowall. 1984. Cryo-electron microscopy of viruses. *Nature.* 308:32–36.

Astbury, W. T., and W. A. Sisson. 1935. X-ray studies of the structure of hair, wood, and related fibres. III: The configuration of the keratin molecule and its orientation in the biological cell. *Proc. Roy. Soc. Lond. A* 150:533–551.

Astbury, W. T., and H. J. Woods. 1933. X-ray studies of the structure of hair, wool, and related fibres. II. The molecular structure and elastic properties of hair keratin. *Phil. Trans. R. Soc. Lond. A* 232:333–394.

Aubrey, K. L., S. R. Casjens, and G. J. Thomas, Jr. 1992. Secondary structure and interactions of the packaged dsDNA genome of bacteriophage P22 investigated by Raman difference spectroscopy. *Biochemistry.* 31:11835–11842.

Ausubel, F., R. Brent, R. E. Kingston, D. D. Moore, J. G. Seidman, J. A. Smith, and K. Struhl. 1995. *In* Current protocols in molecular biology, Chap 1, Vol. 1. V. B. Chanda, editor. John Wiley & Sons Inc., New York. 1.11.1–1.11.2.

Avila-Sakar, A. J., and W. Chiu. 1996. Visualization of beta sheets and side chain clusters in 2-dimensional periodic arrays of streptavidin on phospholipid monolayers by electron crystallography. *Biophys. J.* 70:57–68.

Baker, J. S., and J. E. Johnson. 1997. Principles of virus structure determination. *In* Structural biology of viruses. W. Chiu, R. M. Burnett, and R. L. Garcea, editors. Oxford University Press, New York. 38–79.

Blaurock, A. 1975. Bacteriorhodopsin: a trans-membrane pump containing α-helix. *J. Mol. Biol.* 93:139–158.

Böttcher, B., and R. A. Crowther. 1996. Difference imaging reveals ordered regions of RNA in turnip yellow mosaic virus. *Structure.* 4:387–394.

Böttcher, B., S. A. Wynne, and R. A. Crowther. 1997. Determination of the fold of hepatitis B virus core protein by electron cryo-microscopy. *Nature.* 386:88–91.

Boulin, C. J., R. Kempf, A. Gabriel, and M. H. J. Koch. 1988. Data acquisition systems for linear and area x-ray detectors using delay line readout. *Nucl. Instr. Meth. Phys. Res.* A269:312–320.

Brink, J., and W. Chiu. 1991. Contrast analysis of cryo-images of *n*-paraffin recorded at 400 kV out to 2.1 Å resolution. *J. Microsc.* 161: 279–295.

Bullough, P. A., and P. A. Tulloch. 1990. High-resolution spot-scan electron microscopy of microcrystals of an a-helical coiled-coil protein. *J. Mol. Biol.* 215:161–173.

Chiu, W., R. M. Burnett, and R. L. Garcea. 1997. Structural biology of viruses. W. Chiu, R. M. Burnett, and R. L. Garcea, editors. Oxford University Press, New York.

Conway, J. F., N. Cheng, A. Zlotnick, P. T. Wingfield, S. J. Stahl, and A. C. Steven. 1997. Visualization of the 4-helix bundle in the hepatitis B virus capsid by cryo-electron microscopy. *Nature.* 386:91–94.

Downing, K. H. 1991. Spot-scan imaging in transmission electron microscopy. *Science.* 251:53–59.

Downing, K. H., and W. Chiu. 1990. Cold stage design for high resolution electron microscopy of biological materials. *Electron Microsc. Rev.* 3:213–226.

Downing, K. H., and D. Grano. 1982. Analysis of photographic emulsions for electron microscopy of two-dimensional crystalline specimens. *Ultramicroscopy.* 7:384–404.

Dubochet, J., M. Adrian, J. J. Chang, J. C. Homo, J. Lepault, A. W. McDowall, and P. Schultz. 1988. Cryo-electron microscopy of vitrified specimens. *Q. Rev. Biophys.* 21:129–228.

Earnshaw, W., S. Casjens, and S. C. Harrison. 1976. Assembly of the head of bacteriophage P22: X-ray diffraction from heads, proheads and related structures. *J. Mol. Biol.* 104:387–410.

Earnshaw, W., and S. C. Harrison. 1977. DNA arrangement in isometric phage heads. *Nature.* 268:598–602.

Erickson, H. P. 1973. The Fourier transform of an electron micrograph: first order and second order theory of image formation. *Adv. Opt. Elec. Microsc.* 5:163–199.

Erickson, H. P., and A. Klug. 1970. The Fourier transform of an electron micrograph: effects of defocussing and aberrations, and implications for the use of underfocus contrast enhancement. *Phil. Trans. Roy. Soc. Lond. B* 261:105–118.

Frank, J. 1973. The envelope of electron microscopic transfer functions for partially coherent illumination. *Optik.* 38:519–536.

Frank, J. 1975. Averaging of low exposure electron micrographs of non-periodic objects. *Ultramicroscopy* 1:159–162.

Frank, J. 1976. Determination of source size and energy spread from electron micrographs using the method of Young's fringes. *Optik.* 44: 379–391.

Gabriel, A. 1977. Position sensitive x-ray detector. *Rev. Sci. Instrum.* 48:1303–1305.

Gabriel, A., F. Dauvergne, and G. Rosenbaum. 1978. Linear circular and two dimensional position sensitive detectors. *Nucl. Instr. Meth.* 152: 191–194.

Glaeser, R. M. 1971. Limitations to significant information in biological electron microscopy as a result of radiation damage. *J. Ultrastruct. Res.* 36:466–482.

Glaeser, R. M. 1982. Electron microscopy. *In* Methods of Experimental Physics. G. Ehrenstein and H. Lecar, editors. Vol. 20. Academic Press, Inc., New York. 391–444.

Glaeser, R. M. and K. H. Downing. 1992. Assessment of resolution in biological electron crystallography. *Ultramicroscopy.* 47:256–265.

Greene, B. and J. King. 1996. Scaffolding mutants identifying domains required for P22 procapsid assembly and maturation. *Virology.* 225: 82–96.

Grimes, J. M., J. Jakana, M. Ghosh, A. K. Basak, P. Roy, W. Chiu, D. I. Stuart, and B. V. V. Prasad. 1997. An atomic model of the outer layer of the bluetongue virus core derived from x-ray crystallography and electron cryomicroscopy. *Structure.* 5:885–893.

Hanszen, K. J., and L. Trepte. 1971. Die kontrastubertragung im Elecktonmikroskop bei partiell koharenter beleuchtung. *Optik.* 33:166–182.

Harrison, S. C. 1969. Structure of tomato bushy stunt virus I. The spherically averaged electron density. *J. Mol. Biol.* 42:457–483.

Henderson, R. 1975. The structure of the purple membrane from *Halobacterium halobium:* Analysis of the x-ray diffraction pattern. *J. Mol. Biol.* 93:123–138.

Henderson, R. 1992. Image contrast in high-resolution electron microscopy of biological macromolecules: TMV in ice. *Ultramicroscopy.* 46:1–18.

Henderson, R. 1995. The potential and limitations of neutrons, electrons and x-rays for atomic resolution microscopy of unstained biological molecules. *Q. Rev. Biophys.* 28:171–193.

Henderson, R., J. M. Baldwin, K. H. Downing, J. Lepault, and F. Zemlin. 1986. Structure of purple membrane from *Halobacterium halobium*: recording, measurement and evaluation of electron micrographs at 3.5 Å resolution. *Ultramicroscopy.* 19:147–178.

Henderson, R., and R. M. Glaeser. 1985. Quantitative analysis of image contrast in electron micrographs of beam-sensitive crystals. *Ultramicroscopy.* 16:139–150.

Jack, A., and S. C. Harrison. 1975. On the interpretation of small-angle x-ray solution scattering from spherical viruses. *J. Mol. Biol.* 99:15–25.

Jack, A., S. C. Harrison, and R. A. Crowther. 1975. Structure of tomato bushy stunt virus II. Comparisons of results obtained by electron microscopy and x-ray diffraction. *J. Mol. Biol.* 97:163–172.

Jakubowski, U., W. Baumeister, and R. M. Glaeser. 1989. Evaporated carbon stabilizes thin, frozen-hydrated specimens. *Ultramicroscopy.* 31: 351–356.

Jeng, T. W., W. Chiu, F. Zemlin, and E. Zeitler. 1984. Electron imaging of crotoxin complex thin crystal at 3.5 Å. *J. Mol. Biol.* 175:93–97.

Jeng, T. W., R. A. Crowther, G. Stubbs, and W. Chiu. 1989. Visualization of alpha-helices in tobacco mosaic virus by cryo-electron microscopy. *J. Mol. Biol.* 205:251–257.

Maniatis, T., J. H. Venable, Jr., and L. S. Lerman. 1974. The structure of Ψ DNA. *J. Mol. Biol.* 84:37–64.

Marquardt, D. W. 1963. An algorithm for least-squares estimation of non-linear parameters. *J. Soc. Indust. Appl. Math.* 11:431–441.

Mimori, Y., I. Yamashita, K. Murata, Y. Fujiyoshi, K. Yonekura, C. Toyoshima, and K. Namba. 1995. The structure of the R-type straight flagellar filament of *Salmonella* at 9 Å resolution by electron cryomicroscopy. *J. Mol. Biol.* 249:69–87.

Müller, K. 1982. Experimental practice. *In* Small Angle X-Ray Scattering. O. Glatter and O. Kratky, editors. Academic Press, London. 215–236.

Pauling, L., and R. B. Corey. 1951. The structure of hair, muscle, and related proteins. *Proc. Nat. Acad. Sci. USA.* 37:261–271.

Perkins, G. A., K. H. Downing, and R. M. Glaeser. 1995. Crystallographic extraction and averaging of data from small image areas. *Ultramicroscopy.* 60:283–294.

Prasad, B. V. V., P. E. Prevelige, E. Marietta, R. O. Chen, D. Thomas, J. King, and W. Chiu. 1993. Three-dimensional transformation of capsids associated with genome packaging in a bacterial virus. *J. Mol. Biol.* 231:65–74.

Press, W. H., S. A. Teukolsky, W. T. Vetterling, and B. P. Flannery. 1994. Numerical recipes in C: The art of scientific computing. 2nd ed., Cambridge University Press, New York.

Prevelige, P. E., T. J. Dennis, and J. King. 1988. Scaffolding protein regulates the polymerization of P22 coat subunits into icosahedral shells in vitro. *J. Mol. Biol.* 202:743–757.

Prevelige, P. E., Jr., D. Thomas, J. King, S. A. Towse, and G. J. Thomas, Jr. 1990. Conformational states of the bacteriophage P22 capsid subunit in relation to self-assembly. *Biochemistry.* 29:5626–5633.

Roberts, M. M., J. L. White, M. G. Gratter, and R. M. Burnett. 1986. Three dimensional structure of the adenovirus major coat protein hexon. *Science.* 232:1148–1151.

Schmid, M. F., P. Matsudaira, T. W. Jeng, J. Jakana, E. Towns-Andrews, J. Bordas, and W. Chiu. 1991. Crystallographic analysis of acrosomal bundle from *Limulus* sperm. *J. Mol. Biol.* 221:711–725.

Shaw, A. L., R. Rothnagel, D. Chen, R. F. Ramig, W. Chiu, and B. V. V. Prasad. 1993. Three-dimensional visualization of the rotavirus hemagglutinin structure. *Cell.* 74:693–701.

Sherman, M. B., J. Brink, and W. Chiu. 1996. Performance of a slow-scan CCD camera for macromolecular imaging in a 400 keV electron cryomicroscope. *Micron.* 27:129–139.

Smith, M. F., and J. P. Langmore. 1992. Quantitation of molecular densities by cryo-electron microscopy. *J. Mol. Biol.* 226:763–774.

Stewart, P. L., R. M. Burnett, M. Cyrklaff, and S. D. Fuller. 1991. Image reconstruction reveals the complex molecular organization of adenovirus. *Cell.* 67:145–154.

Stewart, P. L., S. D. Fuller, and R. M. Burnett. 1993. Difference imaging of adenovirus: bridging the resolution gap between x-ray crystallography and electron microscopy. *EMBO J.* 12:2589–2599.

Thomas, G. J., Jr., Y. Li, M. T. Fuller, and J. King. 1982. Structural studies of P22 phage, precursor particles and proteins by laser Raman spectroscopy. *Biochemistry.* 21:3866–3878.

Thuman-Commike, P. A., and W. Chiu. 1995. Automatic detection of spherical particles from spot-scan electron microscopy images. *J. Micros. Soc. Amer.* 1:191–201.

Thuman-Commike, P. A., and W. Chiu. 1996. *PTOOL*: A software package for the selection of particles from electron cryomicroscopy spot-scan images. *J. Struct. Biol.* 116:41–47.

Thuman-Commike, P. A., B. Greene, J. Jakana, B. V. V. Prasad, J. King, P. E. Prevelige, Jr., and W. Chiu. 1996. Three-dimensional structure of scaffolding-containing phage P22 procapsids by electron cryomicroscopy. *J. Mol. Biol.* 260:85–98.

Toyoshima, C., and P. N. T. Unwin. 1988. Contrast transfer for frozen-hydrated specimens: Determination from pairs of defocused images. *Ultramicroscopy.* 25:279–292.

Toyoshima, C., and K. Yonekura. 1993. Contrast transfer for frozen-hydrated specimens II. Amplitude contrast at very low frequencies. *Ultramicrosopy,* 48:165–176.

Trus, B. L., R. B. Roden, H. L. Greenstone, M. Vrhel, J. Schiller, and F. P. Booy. 1997. Novel structural features of bovine papillomavirus capsid revealed by a three dimensional reconstruction to 9 Å resolution. *Nature Struct. Biol.* 4:411–418.

Tsuruta, H., S. Brennan, Z. U. Rek, T. C. Irving, W. H. Tompkins, and K. O. Hodgson. 1998. A wide bandpass multilayer monochromator for biological small angle scattering and diffraction. *J. Appl. Phys*.31: 672–682.

Tuma, R., P. E. Prevelige, Jr., and G. J. Thomas, Jr. 1996. Structural transitions in the scaffolding and coat proteins of P22 virus during assembly and disassembly. *Biochemistry.* 35:4619–4627.

Unwin, P. N. T. 1993. Nicotinic acetylcholine receptor at 9 Å resolution. *J. Mol. Biol.* 229:1101–1124.

Unwin, P. N. T., and R. Henderson. 1975. Molecular structure determination by electron microscopy of unstained crystalline specimens. *J. Mol. Biol.* 94:425–440.

Wade, R. H., and J. Frank. 1977. Electron microscope transfer functions for partially coherent axial illumination and chromatic defocus spread. *Optik.* 49:81–92.

Zhou, Z. H., S. Hardt, B. Wang, M. B. Sherman, J. Jakana and W. Chiu. 1996. CTF determination of images of ice-embedded single particles using a graphics interface. *J. Struct. Biol.* 116:216–222.

Zhou, Z. H., B. V. V. Prasad, J. Jakana, F. Rixon, and W. Chiu. 1994. Protein subunit structures in the herpes simplex virus A-capsid determined from 400 kV spot-scan electron cryomicroscopy. *J. Mol. Biol.* 242:458–469.

Zhu, J., P. A. Penczek, R. Schroder, and J. Frank. 1997. Three-dimensional reconstruction with contrast transfer function correction from energy-filtered cryoelectron micrographs: procedure and application to the 70S *Escherichia coli* ribosome. *J. Struct. Biol.* 118:197–219.

Zlotnick, A., N. Cheng, J. F. Conway, F. P. Booy, A. C. Steven, S. J. Stahl, and P. T. Wingfield. 1996. Dimorphism of hepatitis B virus capsids is strongly influenced by the C-terminus of the capsid protein. *Biochemistry.* 35:7412–7421.